

1 Large scale *in vivo* acquisition, segmentation, and 3D reconstruction of cortical
2 vasculature using open-source functional ultrasound imaging platform.

3
4 Anoek Strumane¹, Théo Lambert^{2,3,4,5}, Jan Aelterman^{1,6}, Danilo Babin¹, Wilfried Philips¹, Gabriel
5 Montaldo^{2,3,4,5}, Clément Brunner^{2,3,4,5,+}, Alan Urban^{2,3,4,5,+,*}

6
7 ¹ Department of Telecommunications and Information Processing - Image Processing and
8 Interpretation, Ghent University-imec, Ghent, Belgium.

9 ² Neuro-Electronics Research Flanders, Leuven, Belgium.

10 ³ Vlaams Instituut voor Biotechnologie, Leuven, Belgium.

11 ⁴ Interuniversity micro-electronic center, Leuven, Belgium.

12 ⁵ Department of Neuroscience, KU Leuven, Leuven, Belgium.

13 ⁶ Department of Physics and Astronomy, Radiation Physics, Ghent University, Ghent, Belgium.

14 + Shared last authorship

15
16 * Corresponding author: alan.urban@nerf.be

17 18 **Abstract**

19 The brain is composed of a dense and ramified vascular network comprising various sizes of arteries,
20 veins, and capillaries. One way to assess the risk of cerebrovascular pathologies is to use
21 computational models to predict the physiological effects of a reduction of blood supply and correlate
22 these responses with observations of brain damage. Therefore, it is crucial to establish a detailed 3D
23 organization of the brain vasculature, which could be used to develop more accurate *in silico* models.
24 For this purpose, we have adapted our open-access functional ultrasound imaging platform previously
25 designed for recording brain-wide activity that is now capable of fast and reproducible acquisition,
26 segmentation, and reconstruction of the cortical vasculature. For the first time, it allows us to digitize
27 the cortical vasculature in awake rodents with a $\sim 100 \mu\text{m}^3$ spatial resolution. Contrary to most
28 available strategies, our approach can be performed *in vivo* within minutes. Moreover, it is easy to
29 implement since it neither requires exogenous contrast agents nor long post-processing time. Hence,
30 we performed a cortex-wide reconstruction of the vasculature and its quantitative analysis, including i)
31 classification of descending arteries versus ascending veins in more than 1500 vessels/animal, ii)
32 quick estimation of their length. Importantly, we confirmed the relevance of our approach in a model of
33 cortical stroke, which enables quick visualization of the ischemic lesion. This development contributes
34 to extending the capabilities of ultrasound neuroimaging to understand better cerebrovascular
35 pathologies such as stroke, vascular cognitive impairment, and brain tumors and is highly scalable for
36 the clinic.

37 38 **Keywords**

39 Brainwide ultrasound imaging, Brain vasculature, Blood vessel segmentation, Stroke

40 **Introduction**

41 Functional ultrasound imaging is a cutting-edge neuroimaging modality suited to track subtle
42 hemodynamic changes, as a proxy for neuronal activity (Macé et al., 2011). So far, the extraction of
43 the functional ultrasound signal mostly relies on the integration of multiple cerebral vessels (i.e.,
44 penetrating arteries, capillaries, and ascending veins) in user-defined (Urban et al., 2014, 2015b),
45 anatomic-based (Sieu et al., 2015) or single-voxel region of interests (Aydin et al., 2020), based on the
46 local change of red blood cells velocity (Urban et al., 2014, 2015a; Brunner et al., 2022) or threshold
47 activity (Urban et al., 2014, 2015b; Gesnik et al., 2016) and recently on reference mouse (Macé et al.,
48 2018; Brunner et al., 2020, 2021; Sans-Dublanc et al., 2021) and rat brain atlas (Vidal et al., 2021;
49 Brunner et al., 2022). Furthermore, these approaches require a mixing of the blood signal coming from
50 distinct vessels with various functions. Indeed, arteries, arterioles, capillaries, venules, and veins
51 behave and adapt differently to neighboring activity (Shih et al., 2013; Rungta et al., 2021) and general
52 cerebrovascular autoregulation along the cerebrovascular tree, not only in the cortex but also in
53 deeper brain structures (Fantini et al., 2016) - a reality rarely addressed when using ultrasound as
54 neuroimaging modality.

55
56 Another great advantage of the used methods is that using Doppler shift in the functional ultrasound
57 images allows for the discrimination of flow directionality without the need for a contrast agent (Macé
58 et al., 2011; Brunner et al., 2022). The extractions of the cerebral vessels from these images would
59 provide more precise information regarding the density of ascending veins and penetrating arteries,
60 the cerebrovascular tree and would support a better characterization of the hemodynamic responses.

61
62 This work proposes to extract the cortex-wide vascular tree from a set of brain-wide angiography
63 captured with the functional ultrasound imaging modality. Existing work for complete vessel network
64 extraction relies on dedicated angiography modalities like magnetic resonance angiography (MRA;
65 Hilbert et al., 2020; Tetteh et al., 2020) or optical coherence tomography (OCT; (Yousefi et al., 2015;
66 Li et al., 2017; Wu et al., 2019). The work by (Cohen et al., 2018) demonstrates that vessel extraction
67 is doable using ultrasound imaging as well, albeit for single vessels that connect to a user-defined
68 point of interest. Other work has demonstrated the extraction of the elliptical intersection of vessels
69 from ultrasound imagery (Guerrero et al., 2007; Wu et al., 2019). A generalized pixel profiling (Babin et
70 al., 2012) and center line extraction procedure (Babin et al., 2018) have proven to robustly detect and
71 extract vessel structures from computed tomography angiography and 3D rotational angiography
72 images.

73
74 The ideas behind these last two works (Babin et al., 2012, 2018) are the basis of the vessel extraction
75 of this work. The final method robustly estimates the extent to which individual voxels adhere to the
76 properties of vessels, extracts those that are most likely to be part of vessels and subsequently
77 extracts their centerline to form a 3D skeleton which allows for the analysis of the blood vessel's
78 morphological characteristics. Such processing is of interest in biomedical image processing, as the
79 morphological characteristics like diameter, tortuosity, and shape of blood vessels are critical for early
80 diagnosis, treatment planning, and evaluation.

81 **Materials and Methods**

82 **Animals**

83 The rats analysed in this work have been selected from the dataset generated for Brunner et al., 2022.
84 Experimental procedures were approved by the Committee on Animal Care of the Catholic University
85 of Leuven, in accordance with the national guidelines on the use of laboratory animals and the
86 European Union Directive for animal experiments (2010/63/EU). Adult male Sprague-Dawley rats
87 (n=9; Janvier Labs, France) with an initial weight between 200-300g were housed in standard
88 ventilated cages and kept in a 12:12hrs reverse dark/light cycle environment at a temperature of 22°C
89 with *ad libitum* access to food and water.

90

91 **Cranial window for brain-wide imaging.**

92 The surgical procedure has been previously described in Brunner et al., 2022. Briefly, the cranial
93 window was performed in rats under isoflurane anesthesia (Induction 5%, Surgery 2.0-2.5%, Imaging
94 1.5% in compressed dry air delivered at 0.6l/min; Iso-Vet, Dechra, Belgium). Xylocaine (0.5%,
95 AstraZeneca, England) was injected subcutaneously into the head skin as pre-operative analgesia.
96 The scalp was shaved and cleaned with iso-betadine before being removed over the entire dorsal
97 skull. The cranial window extended from bregma +4.0 to -7.0mm antero-posterior and \pm 6.0mm away
98 from the midline. The skull was carefully removed without damaging the dura. The brain was covered
99 with a low-melting 2% agarose (Sigma-Aldrich, USA) and ultrasound gel to ensure a proper acoustic
100 coupling with the ultrasound probe.

101

102 **2D scans of the brain vasculature with ultrasound imaging.**

103 The brain-wide imaging procedure has been previously described in Brunner et al., 2022. Briefly, the
104 functional ultrasound imaging scanner is equipped with custom acquisition and processing software
105 described by Brunner et al., 2021. In short, the scanner is composed of a linear ultrasonic transducer
106 (15MHz, 128 elements, Xtech15, Vermon, France) connected to 128-channel emission-reception
107 electronics (Vantage, Verasonics, USA) that are both controlled by a high-performance computing
108 workstation (fUSI-2, AUTC, Estonia). The transducer was motorized (T-LSM200A, Zaber Technologies
109 Inc., Canada) to allow antero-posterior scanning of the brain. Imaging is performed on an anti-vibration
110 table to minimize external sources of vibration.

111

112 The acquisition consisted in cross-section coronal μ Doppler image (12.8-mm width, 9-mm depth)
113 composed of 300 compound images acquired at 500Hz. Each compound image is computed by
114 adding nine plane-wave (4.5kHz) with angles from -12° to 12° with a 3° step. The blood signal was
115 extracted from 300 compound images using a single value decomposition filter and removing the 30
116 first singular vectors (Urban et al., 2015a). The μ Doppler image is computed as the mean intensity of
117 the blood signal in these 300 frames that is an estimator of the cerebral blood volume (CBV; Macé et
118 al., 2011, 2013). This sequence enables a temporal resolution of 0.6s, an in-plane resolution of
119 100x110 μ m, and an off-plane (thickness of the image) of ~300 μ m (Brunner et al., 2021). We
120 performed high-resolution 2D scans of the brain vasculature consisting of 89 coronal planes from
121 bregma (B) +4.0 to -7.0mm spaced by 0.125mm (**Figure 1**, Step 1).

122

123 **Stroke**

124 The cortical stroke was induced by the mechanical and permanent occlusion of both the left common
125 carotid artery (CCA) and the distal branch of the left middle cerebral artery (MCA). The post-stroke 2D
126 scan of the rat brain vasculature was performed 70min after the stroke onset. The ultrasound probe
127 was remained in the exact same position between the 2 scans. The procedure to induce the cortical
128 stroke is detailed in Brunner et al., 2022.

129

130 **Data processing and analysis**

131 The μ Doppler image is acquired and then processed in a cascade of steps: We start with an overview
132 of these steps before explaining in more detail:

133

- 134 1. Step 1: Acquisition of micro-Doppler images of brain vasculature (**Figure 1**, Step 1).
 - 135 a. Optional: Color-Doppler filter to separate arteries and veins
- 136 2. Step 2: Vessel extraction and skeletonization (**Figure 1**, Step 2).
 - 137 a. Step 2A: Detection of tubular structures using generalized R-profiling: in μ Doppler
138 images, vessels appear as a connected series of voxels that are brighter than their
139 surroundings, called ridges. Generalized R-profiling finds and enhances these ridges,
making them more suitable for extraction by thresholding.

- 140 b. Step 2B: Filtering of segmented vessels: the enhanced ridges, which indicate vessels,
141 are thresholded to extract foreground voxels. These foreground voxels represent the
142 extracted vessels. As an additional filtering step, isolated foreground voxels, which are
143 most likely to represent noise, are removed.
144 c. Step 2C: Skeletonization of the complete brain: the centerlines of the extracted
145 vessels are determined, and a graph type skeleton is built along these lines.
146 3. Step 3: Analysis of the cortical brain vasculature (**Figure 1**, Step 3).
147 a. 3A: Manual specification of plane of interest: a line is drawn in the coronal cross-
148 section μ Doppler images of the brain indicating the location of vessels of interest. This
149 line is extended to a plane reaching from posterior to anterior
150 b. 3B: Extraction of vessels traversing plane of interest
151 c. 3C: Counting of the number of vessels
152 d. 3D: Analysis of vessel length distribution

153 The most complex data processing steps are steps 2A and 2C, which we now explain in greater detail.

154 **Detection of tubular structures using generalized R-profiling**

155 The goal of “Step 2A: Detection of tubular structures using generalized R-profiling” is to calculate per-
156 voxel measures that express how contrasted a voxel is compared to its multi-scale neighborhood. We
157 achieve this by comparing the voxel gray value to the values found in its neighborhoods (for different
158 sizes). This is based on the *R-profiling* approach described in Babin et al., 2018. The neighborhoods
159 used in this paper are spherical structures with a radius ranging from 1 voxel to 5 voxels, chosen to
160 correspond to the radius of the largest vessels. From each sphere of radius r , the sphere of size $r-1$ is
161 subtracted, to result in a differential spherical structure. The new voxel value (called the profile
162 measure) is the number of consecutive neighborhoods (for increasing size of neighborhoods) for
163 which the current voxel is brighter than or as bright as its neighborhood. For example, this brightness
164 can be defined as the mean voxel gray value of a neighborhood. The voxel gray value of a central
165 voxel is then compared to the mean gray value of its neighborhood of radius $r = 1$ and if it is greater
166 than or equal to this mean value, the process is repeated for $r=2$ and so forth. The largest radius for
167 which this condition is fulfilled (up to the maximum value $r=5$), becomes the new voxel value (**Figure**
168 **1**, Step 2A).
169

170 The brightness that is associated with a neighborhood may be chosen using a variety of basic
171 aggregation operators for the neighborhood's voxel values like mean, maximum, minimum, median,
172 etc. The choice of these operators is made by considering both the properties of the image (such as
173 noise and artifacts) and the type of structures that need to be extracted. It is even possible to define
174 the operator as the average of multiple other operators. The chosen operator is called the profile
175 function.
176

177 As the goal of this paper is to extract and analyze vessels, an operator that promotes the ridge-like
178 appearance of vessels is defined. The different basic profile functions that were used are listed below:

- 179 1. Maximum: the maximum value,
- 180 2. Median (+): the median, taking the highest value if there are two medians,
- 181 3. Median (-): the median, taking the lowest value if there are two medians,
- 182 4. Minmax average: the mean of the minimum and maximum,
- 183 5. Minmax root: the root of the multiplication of the minimum and maximum,
- 184 6. Median root: the root of the multiplication of median (+) and median (-).

185 To evaluate robustness when gathering analytical information, three different operator functions are
186 used on each rat. These three operator functions were respectively an average of the following three
187 combinations: [1,2,3], [1,4,5], and [1,5,6].
188

189 Applying these three different profile functions on a μ Doppler image of a rat brain results in three 3D
190 images with voxel values ranging from 0 to 5, where the detected vessel-like structures have a higher
191 value than the non-vessels. These images are now ready to be thresholded to result in an extraction of
192 the detected vessel-like structures.
193

194 **Skeleton creation**

197 To extract the centerline of the resulting vessels, ordered skeletonization is applied as proposed in
198 Babin et al., 2012. For all foreground voxels, the Euclidian distance to its nearest background voxel is
199 determined. The voxels are then sorted by their respective distances in an ascending order. The
200 voxels are iterated over in this order and a voxel is removed if considered redundant to maintain
201 skeletal connectivity. In other words, a central voxel is redundant in its 27- neighborhood if removing it
202 does not change the number of connected components in that neighborhood. The remaining
203 foreground voxels represent the centerlines of the extracted vessels.
204

205 The remaining foreground voxels in the centerline image are subsequently labeled according to their
206 number of foreground neighbors, yielding the following label values (**Figure 1**, Step 2C):

- 207 • 0: represents an isolated voxel and is not considered further,
- 208 • 1: represents an endpoint of a vessel, and will be represented as a node in the graph-
209 type skeleton,
- 210 • 2: represents a part of a vessel, and will be represented as a link in the graph-type
211 skeleton,
- 212 • >2: corresponds to a vessel bifurcation. All connected voxels with a degree larger than
213 two represent a single vessel bifurcation. The geometric median of these voxels is used
214 as the location of the bifurcation, thus resulting in a single node in the graph-type
215 skeleton.
216

217 The resulting graph consists of vessel endpoints or bifurcations represented by nodes and vessel
218 branches represented by links.
219

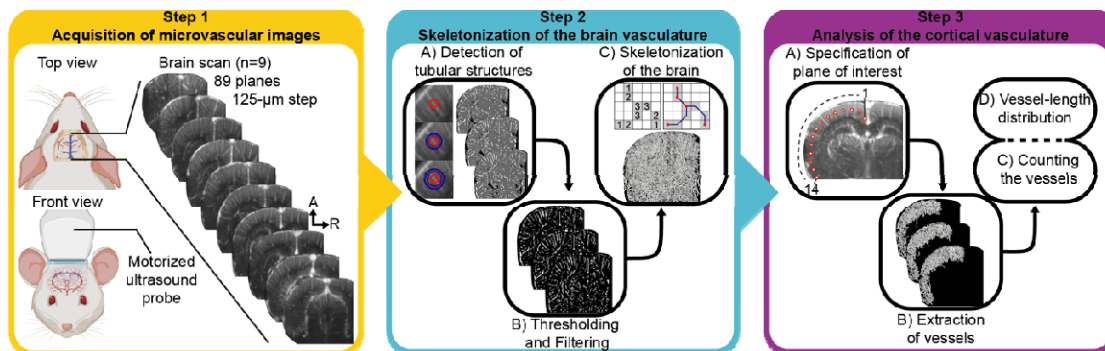


Figure 1. Experimental procedure of whole-brain ultrasound imaging scan of the rat cerebral vasculature (Step 1, yellow), framework for center line extraction and vessel skeletonization (Step 2, blue) and analysis of the cortical vasculature (Step 3, purple). Steps are detailed in the Material and Methods section.

221 **Results**

222 In this study, we have segmented the rat brain vasculature based on the μ Doppler signal captured
223 with ultrasound imaging. We have automatically reconstructed a 3D skeleton of the entire cerebral
224 microvasculature (**Figure 1**). We then extended the analysis to identify and classify individual cortical
225 vessels as penetrating arterioles or ascending venules based on their flow directionality away or
226 toward the ultrasound transducer, respectively (**Figure 2**). Finally, we performed the 3D reconstruction
227 of the cortical microvasculature in a pathological context of cortical stroke (**Figure 3**). The global
228 procedure from brain-wide scan, vessel extraction, and analysis is depicted in **Movie 1**.
229

230 **Ultrasound imaging for skeletonization of the cortical vasculature.**

231 Brain-wide imaging was carried out in head-fixed anesthetized rats (n=9) directly after being subjected
232 to cranial window surgery. An angiographic scan composed of a set of 89 μ Doppler coronal slices,
233 spaced by 0.125 mm, was performed using a motorized ultrasound transducer (**Figure 1**, Step 1).
234 From this brain-wide scan, we have extracted individual coronal cross-section of μ Doppler image
235 based on the relative CBV signal (**Figure 2A** and **Movie 1**). Then, we have skeletonized the brain
236 vasculature following the cascade of image processing steps described in the methods section
237 (**Figure 1**, Step 2). The resulting structure is a 3D skeleton of all the vessels in the brain that were in
238 the field of view of the ultrasound probe. Vessels of interest, specifically the cortical vessels of the left
239 hemisphere, were then extracted by means of a user-defined plane of interest positioned below the
240 brain surface (**Figures 1-3A, 1-3B, 2D** and **Movie 1**). To count the number of vessels in the extracted
241 region of the brain, the plane of interest was divided into 14 sections of equal length in the medio-
242 lateral direction. Per section, the vessels traversing their region of the plane of interest were counted
243 (**Figure 1-3C**). These vessel counts are prone to a slight error, as longer vessels can pass through the
244 plane of interest in more than one of these sections, resulting in a slight overestimation of the total
245 number of vessels. A similar source of slight error is that the point spread function causes some
246 vessels to be detected in multiple planes of interest due to its blurring effect. To determine the
247 distribution of the vessel lengths, the pixel length of each vessel in the extracted skeleton of interest
248 was calculated (**Figure 1-3D**). Because the voxel size in the μ Doppler coronal images is anisotropic,
249 this pixel length should not be interpreted as a one-to-one map to the actual vessel's length, but rather
250 a correlated quantity. The exact measurement of the length remains limited by the anisotropic
251 resolution of the ultrasound imaging voxel technique.
252

253 The Doppler measurements allow to generate color-coded images based on the blood flow
254 directionality (**Figure 2B**) as well. This representation of the brain microvasculature allows for the
255 vessel discrimination between penetrating arteries and ascending veins in the cortex. Still, the Doppler
256 measurement is not perfectly accurate and does not result in a 3D velocity vector for the flow, rather
257 yielding a projection of the vector. this nonetheless results in two separate images, one clearly
258 depicting the penetrating arteries, the other the ascending veins. These two images were separately
259 processed in the same manner as the original μ Doppler images (i.e., with no separation between
260 veins and arteries). The resulting vein and artery skeletons were overlaid to visualize the
261 combination of both (**Figure 2E**). Due to the aforementioned resolution issues, the same vessels can
262 appear in both images, resulting in the vessel being counted as both a vein and an artery. For this
263 reason, the total number of veins and arteries is slightly overestimated.
264

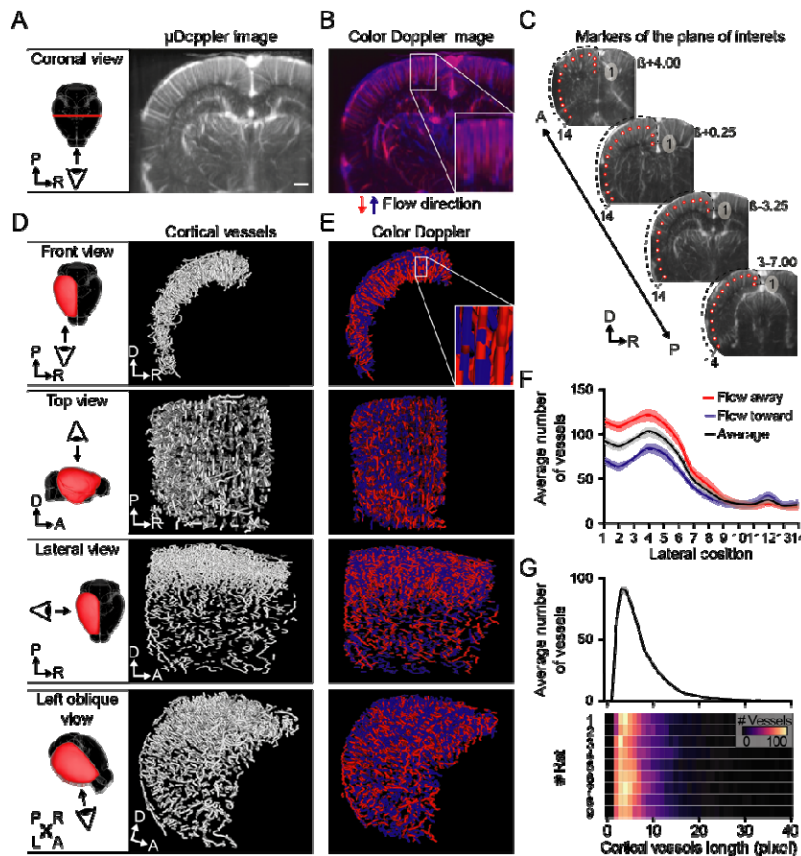


Figure 2. (A) Coronal cross-section μ Doppler image and (B) color-coded image depicting flow directionality toward (blue) or away from (red) the ultrasound probe extracted from the same brain scan. (C) Position of markers (1 to 14 from medial to lateral) used to perform the vessel extraction. (D) Front, top, lateral, and left-oblique views (top to bottom) of the 3D volume-rendered skeleton of all and (E) flow-discriminated cortical vessels. (F) Average number of cortical vessels (mean \pm sem) and (G) average (top; mean \pm sem, $n=9$) and individual distribution (bottom) of cortical vessel length. R, right; L, left; P, posterior; A, anterior; D, dorsal. Scale bar: 1mm.

265

266

267

268

269

270

271

272

273

274

275

276

277

278

279

280

From this processing we have counted 892.6 ± 57.5 cortical penetrating arteries (i.e., flow direction away from the ultrasound probe; mean \pm sem, $n=9$) and 641.7 ± 53.1 cortical ascending veins (i.e., flow direction toward the ultrasound probe; mean \pm sem, $n=9$). We have observed an unequal distribution of cortical vessels along the medio-lateral plane of interest ranging from 114.6 ± 5.2 cortical penetrating arteries medially (i.e., position 1) to 18.0 ± 3.9 laterally (i.e., position 14; **Figure 2F**, red plot) and respectively 71.6 ± 4.4 and 23.0 ± 5.1 for ascending veins (**Figure 2F**, blue plot). The medio-lateral variability can be explained by i) the uncertainty of the speed estimator in the estimation of flow directionality (see zoom-in views of color Doppler image in **Figure 2B** and skeleton in **Figure 2E**), and ii) the probe-to-cortical vessel angle potentially affecting the detection of flow directionality (Brunner et al., 2022). However, the number of penetrating and ascending vessels counted along the antero-posterior axis and among animals is highly robust (**Figure 2F**). Moreover, the length of the cortical vessels computed from cortex-wide skeletons follows a beta distribution centered in 3-pixel long vessels (**Figure 2G**, top), representative for all rats processed (**Figure 2G**, bottom).

281

Cortex-wide skeletonization for precise detection of ischemic stroke.

282

283

284

285

286

287

288

289

290

291

292

293

In a second and pathological application of the center line extraction, we have scanned the rat brain 70min after they have been subjected to concomitant CCA+MCA occlusions and performed the skeletonization of the cortical vasculature as described above. The cortical stroke was confirmed by the direct visualization of the coronal cross-section μ Doppler images showing a distinct loss of signal onto the cortex of the left hemisphere when compared with pre-stroke scan (**Figure 3A**, **Supplementary Figure 1**, and **Movie 3**). See details in (Brunner et al., 2022). In a representative case, the skeletonization of the cortical vasculature after stroke allows the precise detection of the ischemic territory (**Figure 3B** and **Movie 3**) and showing a nearly 90% drop in detected vessels at the center of the ischemic regions along the antero-posterior (**Figure 3B**, color-coded line), but is significantly reduced of $\sim 50\%$ between lateral position 6 to 10 (grey curve, **Figure 3C** and **Supplementary Figure 2**; p value $<0.001^{***}$ obtained by ordinary two-way ANOVA and uncorrected Fisher LSD with single pooled variance), i.e., where the vascular territory supplied by the distal branch of the MCA is located.

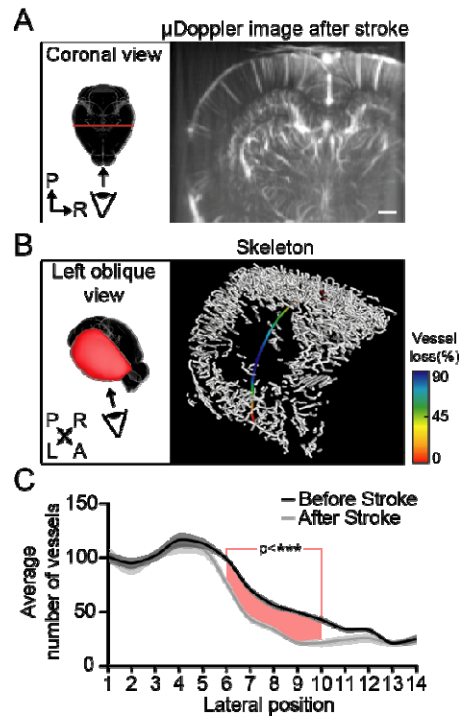


Figure 3. (A) Coronal cross-section μ Doppler image extracted from the brain scan after stroke. This coronal μ Doppler image is at the exact same brain position as in Figure 2A. (B) Left-oblique view of the 3D volume-rendered skeleton of cortical vessels after stroke and average drop in vessels detection along the antero-posterior axis (% of vessel loss; color coded line). (C) Difference of cortical vessels number along the medio-lateral plane of interest before (black) and after stroke (grey). Positions of the medio-lateral plane of interest depicting significant differences (with a p value<0.001***) are highlighted in red. R, right; L, left; P, posterior; A, anterior; D, dorsal. Scale bar: 1mm.

294

295

Discussion

296

297

298

299

300

301

302

303

304

305

306

307

308

309

310

311

312

313

314

315

316

317

318

319

320

321

322

323

324

325

326

327

328

The experimental results show that the μ Doppler ultrasound technique yields imagery of sufficient quality to extract vasculature connectivity through the proposed skeletonization method. This enables subsequent statistical analysis of the extracted vasculature. The extraction of these cortical vessels supports a better characterization of the functional ultrasound imaging signal based on vessel length, density, blood speed and thus also offering the measurement of the cerebral blood flow (CBF).

An observed point-of-attention for the vasculature extraction is an overestimation of the number of vessels. This happens due to three reasons: i) vessels traversing multiple segments of the plane of interest, ii) the spatially varying voxel resolution of the ultrasound imaging technique and iii) the uncertainty of the speed estimator (in the case of separation between veins and arteries). The first cause only has effect when the plane of interest is segmented into multiple regions. This issue will not take place if the total number of vessels of the complete plane is being counted, as every vessel will only be counted once. A way to counteract this over-estimation in the different segments is to only count vessels when they are seen traversing the plane for the first time. However, then the ratio of the vessel density throughout the different segments would be less accurate. The other causes may be mitigated through improved HW resolution and/or multi-image fusion to extract full 3D velocity profiles.

At the current stage, the vessel lengths are given in pixels. These measurements cannot be interpreted as exact values because the pixel size is not isotropic. A solution for this would be to take the direction of vessels into account when calculating their length. Knowing the exact length, width and height of the pixels, these lengths may be directly converted to a more meaningful length metric, rather than number of pixels.

Throughout the processing of the images only one step requires user interaction: the specification of the plane of interest. In future application, this step could be done automatically, making the method even more robust when comparing the results of different rats. For example, a brain segmentation technique could be used to find the outline of the brain, which allows the plane of interest to be placed automatically at a fixed distance from this outline. In this way, once the method has been tuned for its specific application, the process can be done automatically without the need of any user interaction.

In terms of resolvable vessel resolution, the data processing procedure produces results at the resolution of the fUS image, in other words: single-voxel-width vessels may be extracted by this procedure. The processing complexity is dominated by step 2A. This is a numerical procedure of linear

329 time complexity in the number of voxels being processed. The implementation developed for the
330 experiments in this paper takes 4-5 minutes on a single-core CPU platform, for a 2-megapixel voxel
331 fUS image. Specific code optimization and implementation on a parallel computing platform (GPU /
332 FPGA) can realistically be expected to bring this processing time down to the second range, opening
333 the door to interactive, real-time vessel imaging and quantification using the fUSI modality.
334

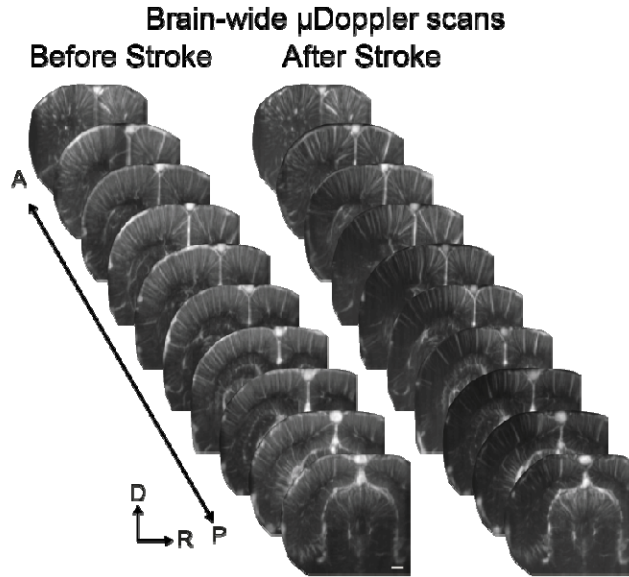
335 A direct application of the center line extraction would be to use the skeletonized brain-wide
336 vasculature as a new strategy to improve the filtering, better characterize the fUSI signal and better
337 understand the cerebral hemodynamics and neurovascular coupling. Indeed, one could use the
338 skeleton as a mask to automatically extract hemodynamic parameters from veins and/or arteries such
339 as cerebral blood volume (CBV), red blood cells velocity and even the cerebral blood flow (CBF) in a
340 straightforward and quantitative parameter. Furthermore, it would also allow for live detection of
341 vessels and hemodynamics in preclinical/clinical context. In the meantime, our 3D reconstruction
342 approach combined with the recent improvement vascular ultrasound super-resolution imaging without
343 contrast agents (Bar-Zion et al., 2021), would allow to better separate the dense and overlapping
344 blood vessels; thus, performing a complementary analysis focusing on 2nd/3rd order arterioles, venules,
345 and capillaries smaller than the resolution of the functional ultrasound imaging modality, but where
346 neurons mostly modulate blood supply (Rungta et al., 2021).
347

348 Moreover, the brain-wide skeleton could help improve the registration by providing a better fit with the
349 reference atlas of the model investigated (Macé et al., 2018; Brunner et al., 2020, 2022; Takahashi et
350 al., 2021) either by the means of vascular landmarks combined with automatic alignment approaches
351 (Nouhoum et al., 2021) or markerless CNN-based deep learning classification (Lambert et al., 2022).
352

353 Several strategies are now allowing for longitudinal monitoring of the brain functions of the same
354 animal which in this context would be of high interest when considering pathologies as the brain
355 vasculature and the associated functions have been shown affected (e.g., angiogenesis, vascular
356 rarefaction, hypertension) in various diseases including Alzheimer's (Meyer et al., 2008; Gutierrez et
357 al., 2016; Zhang et al., 2019; Lowerison et al., 2021; Szu and Obenaus, 2021) and Parkinson's
358 diseases (Yang et al., 2015; Al-Bachari et al., 2020; Biju et al., 2020), tumors (Gambarota et al., 2008;
359 Guyon et al., 2021), obesity (Dorrance et al., 2014; Pétrault et al., 2019; Gruber et al., 2021) currently
360 addressed at the brain-wide scale with either technology offering reduced spatiotemporal resolution
361 (Pathak et al., 2011; Lin et al., 2013) or *post-mortem* strategies (Hlushchuk et al., 2020; Todorov et al.,
362 2020; Bumgarner and Nelson, 2022). In the stroke context, the cortex-wide skeletonization of vessels
363 could also be used as a follow-up strategy for detecting i) progressive and long-lasting
364 neovascularization of the infarcted tissue (Ergul et al., 2012; Liman and Endres, 2012), and ii) stroke-
365 induced of reverse flow (Li et al., 2010; Ergul et al., 2012) both of crucial interest when considering
366 tissue survival and functional recovery of the insulted tissue.
367

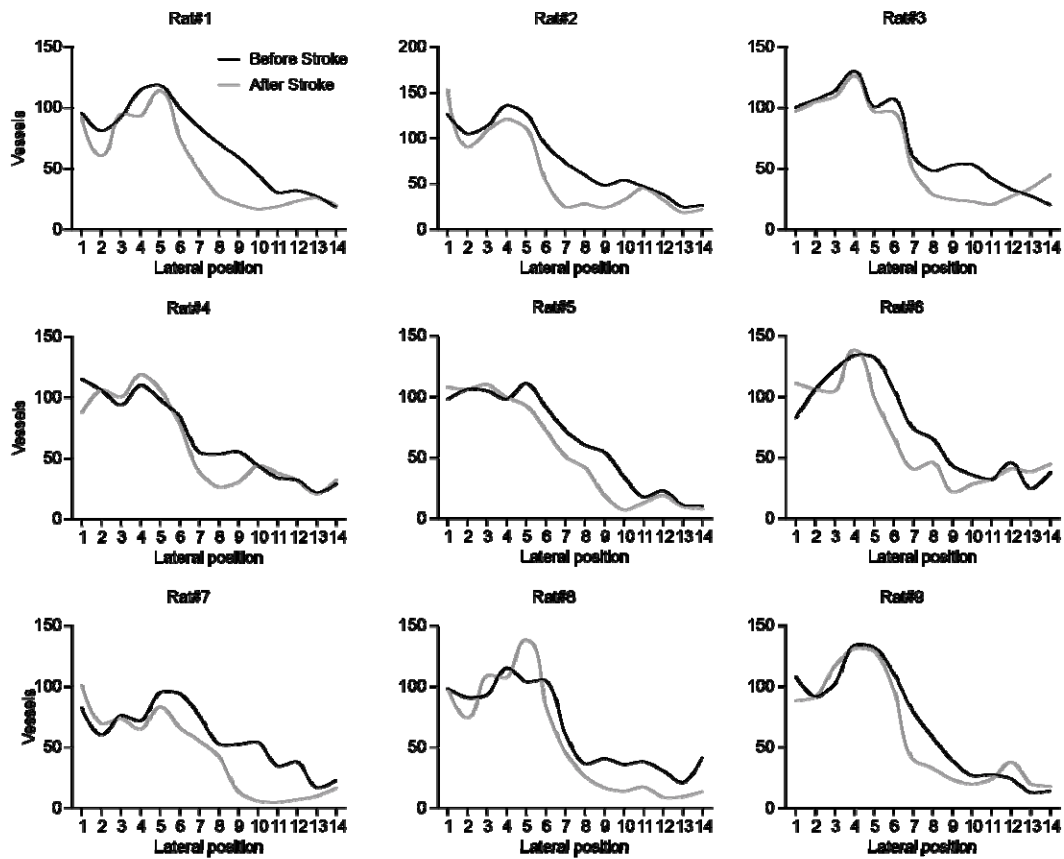
368 This paper validates the digitization of rat brain vasculature from ultrasound imagery without the need
369 for contrast agent. It presents an image processing procedure for extraction of vessel structures that
370 was shown to be robust throughout different test subjects while needing little user interaction. The
371 complete process shows promising results with the possibility of acceleration to work in near real-time.
372 Cortex-wide quantification in terms of vessel number and length and discrimination between veins and
373 arteries was successfully shown. The use of such quantification was demonstrated in the case of
374 ischemic stroke, where a clear drop in number of vessels was observed in the expected region.

375 **Supplementary Information**



Supplementary Figure 1 – Related to Figure 3A-B. μ Doppler scans of the cortical vasculature before and after stroke. Scale bar: 1mm.

376



Supplementary Figure 2 – Related to Figure 3C. Number of cortical vessels along the medio-lateral plane of interest before (black) and after stroke (grey) for every single rat used in this work.

377

378 **Movie 1.** Experimental pipeline from whole-brain ultrasound imaging scan of the rat cerebral
379 vasculature to vessel skeletonization.

380
381 **Movie 2.** 3D volume-rendered skeleton of flow-discriminated cortical arteries (red) and veins (blue).
382

383 **Movie 3.** 3D volume-rendered skeleton before and after cortical stroke.
384

385 **Data Availability Statement**

386 The dataset and code are available on Zenodo and can be downloaded at <https://doi.org/>

387

388 **Author's contribution statement**

389

	Strumane	Lambert	Aelterman	Babin	Philips	Brunner	Urban
Concept		X		X		X	X
Methodology	X	X	X	X		X	X
Software	X			X			X
Imaging						X	
Data Analysis	X		X	X			
Visualization	X					X	
Manuscript	X	X	X	X	X	X	X
Supervision				X		X	X
Funding				X	X		X

390

391 AS: Methodology, Software, Data Analysis, Visualization, Manuscript.

392

392 TL: Concept, Methodology, Manuscript.

393

393 JA: Methodology, Data Analysis, Manuscript.

394

394 DB: Concept, Methodology, Software, Data Analysis, Manuscript, Supervision, Funding.

395

395 WP: Manuscript, Funding.

396

396 CB: Concept, Methodology, Imaging, Visualization, Manuscript, Supervision.

397

397 AU: Concept, Methodology, Software, Manuscript, Supervision, Funding.

398

399

399 **Funding**

400

400 This work is supported by grants from the Foundation Leducq (15CVD02) and KU Leuven
401 (C14/18/099-STYMULATE-STROKE). The functional ultrasound imaging platform is supported by
402 grants from FWO (MEDI-RESCU2-AKUL/17/049, G091719N, and 1197818N), VIB Tech-Watch (fUSI-
403 MICE), Neuro-Electronics Research Flanders TechDev fund (3D-fUSI project). Jan Aelterman was
404 funded funded by the Research Foundation—Flanders in the Strategic Basic Research Programme
405 (FWO-SBO), file number S003418N.

406

407

407 **Acknowledgements**

408

408 We thank all NERF animal caretakers, including I. Eyckmans, F. Ooms, and S. Luijten, for their help
409 with the management of the animals.

410

411

411 **Competing interests**

412

412 A.U. is the founder and a shareholder of AUTC company commercializing functional ultrasound
413 imaging solutions for preclinical and clinical research.

414 **References**

- 415 Al-Bachari, S., Naish, J. H., Parker, G. J. M., Emsley, H. C. A., and Parkes, L. M. (2020).
416 Blood-brain barrier leakage is increased in Parkinson's disease. *Front. Physiol.* 11,
417 593026.
- 418 Aydin, A. K., Haselden, W. D., Goulam Houssen, Y., Pouzat, C., Rungta, R. L., Demené, C.,
419 et al. (2020). Transfer functions linking neural calcium to single voxel functional
420 ultrasound signal. *Nat. Commun.* doi:10.1038/s41467-020-16774-9.
- 421 Babin, D., Pižurica, A., Bellens, R., De Bock, J., Shang, Y., Goossens, B., et al. (2012).
422 Generalized pixel profiling and comparative segmentation with application to
423 arteriovenous malformation segmentation. *Med. Image Anal.* 16, 991–1002.
- 424 Babin, D., Pižurica, A., Velicki, L., Matić, V., Galić, I., Leventić, H., et al. (2018).
425 Skeletonization method for vessel delineation of arteriovenous malformation. *Comput.*
426 *Biol. Med.* 93, 93–105.
- 427 Bar-Zion, A., Solomon, O., Rabut, C., Maresca, D., Eldar, Y. C., and Shapiro, M. G. (2021).
428 Doppler slicing for ultrasound super-resolution without contrast agents. *bioRxiv.*
429 doi:10.1101/2021.11.19.469083.
- 430 Biju, K. C., Shen, Q., Hernandez, E. T., Mader, M. J., and Clark, R. A. (2020). Reduced
431 cerebral blood flow in an α -synuclein transgenic mouse model of Parkinson's disease.
432 *J. Cereb. Blood Flow Metab.* 40, 2441–2453.
- 433 Brunner, C., Grillet, M., Sans-Dublanc, A., Farrow, K., Lambert, T., Macé, E., et al. (2020). A
434 Platform for Brain-wide Volumetric Functional Ultrasound Imaging and Analysis of
435 Circuit Dynamics in Awake Mice. *Neuron.* doi:10.1016/j.neuron.2020.09.020.
- 436 Brunner, C., Grillet, M., Urban, A., Roska, B., Montaldo, G., and Macé, E. (2021). Whole-
437 brain functional ultrasound imaging in awake head-fixed mice. *Nat. Protoc.*
438 doi:10.1038/s41596-021-00548-8.
- 439 Brunner, C., Lagumersindez Denis, N., Gertz, K., Grillet, M., Montaldo, G., Endres, M., et al.
440 (2022). Brain-wide continuous functional ultrasound imaging for real-time monitoring
441 of hemodynamics during ischemic stroke. doi:10.1101/2022.01.19.476904.
- 442 Brunner, C., Macé, E., Montaldo, G., and Urban, A. (2022). Quantitative hemodynamic
443 measurements in cortical vessels using functional ultrasound imaging. *Front.*
444 *Neurosci.* 0. doi:10.3389/fnins.2022.831650.
- 445 Bumgarner, J. R., and Nelson, R. J. (2022). Open-source analysis and visualization of
446 segmented vasculature datasets with VesselVio. *Cell Reports Methods*, 100189.
- 447 Cohen, E., Deffieux, T., Demené, C., Cohen, L. D., and Tanter, M. (2018). "3D vessel
448 extraction in the rat brain from ultrasensitive Doppler images," in *Lecture Notes in*
449 *Bioengineering* (Cham: Springer International Publishing), 81–91.
- 450 Dorrance, A. M., Matin, N., and Pires, P. W. (2014). The effects of obesity on the cerebral
451 vasculature. *Curr. Vasc. Pharmacol.* 12, 462–472.
- 452 Ergul, A., Alhusban, A., and Fagan, S. C. (2012). Angiogenesis. *Stroke* 43, 2270–2274.
- 453 Fantini, S., Sassaroli, A., Tgavalekos, K. T., and Kornbluth, J. (2016). Cerebral blood flow
454 and autoregulation: current measurement techniques and prospects for noninvasive
455 optical methods. *Neurophotonics* 3, 031411.
- 456 Gambarota, G., Leenders, W., Maass, C., Wesseling, P., van der Kogel, B., van Tellingen,
457 O., et al. (2008). Characterisation of tumour vasculature in mouse brain by USPIO
458 contrast-enhanced MRI. *Br. J. Cancer* 98, 1784–1789.
- 459 Gesnik, M., Blaize, K., Dizeux, A., Sahel, J.-A., Fink, M., Deffieux, T., et al. (2016).
460 Spatiotemporal response of rat visual cortex during moving stimuli using Functional
461 Ultrasound (fUS) imaging. in *2016 IEEE International Ultrasonics Symposium (IUS)*
462 (IEEE). doi:10.1109/ultsym.2016.7728612.
- 463 Gruber, T., Pan, C., Contreras, R. E., Wiedemann, T., Morgan, D. A., Skowronski, A. A., et
464 al. (2021). Obesity-associated hyperleptinemia alters the gliovascular interface of the
465 hypothalamus to promote hypertension. *Cell Metab.* 33, 1155-1170.e10.
- 466 Guerrero, J., Salcudean, S. E., McEwen, J. A., Masri, B. A., and Nicolaou, S. (2007). Real-
467 time vessel segmentation and tracking for ultrasound imaging applications. *IEEE*
468 *Trans. Med. Imaging* 26, 1079–1090.

- 469 Gutierrez, J., Honig, L., Elkind, M. S. V., Mohr, J. P., Goldman, J., Dwork, A. J., et al. (2016).
470 Brain arterial aging and its relationship to Alzheimer dementia. *Neurology* 86, 1507–
471 1515.
- 472 Guyon, J., Chapouly, C., Andrique, L., Bikfalvi, A., and Daubon, T. (2021). The normal and
473 brain tumor vasculature: Morphological and functional characteristics and therapeutic
474 targeting. *Front. Physiol.* 12, 622615.
- 475 Hilbert, A., Madai, V. I., Akay, E. M., Aydin, O. U., Behland, J., Sobesky, J., et al. (2020).
476 BRAVE-NET: Fully automated arterial brain vessel segmentation in patients with
477 cerebrovascular disease. *Front Artif Intell* 3, 552258.
- 478 Hlushchuk, R., Haberbür, D., Soukup, P., Barré, S. F., Khoma, O.-Z., Schittny, J., et al.
479 (2020). Innovative high-resolution microCT imaging of animal brain vasculature. *Brain*
480 *Struct. Funct.* 225, 2885–2895.
- 481 Lambert, T., Brunner, C., Kil, D., Wuyts, R., D'Hondt, E., and Urban, A. (2022). A deep
482 learning classification task for accurate brain navigation during functional ultrasound
483 imaging. *bioRxiv*. doi:10.1101/2022.03.18.484747.
- 484 Li, A., You, J., Du, C., and Pan, Y. (2017). Automated segmentation and quantification of
485 OCT angiography for tracking angiogenesis progression. *Biomed. Opt. Express* 8,
486 5604.
- 487 Li, L., Ke, Z., Tong, K. Y., and Ying, M. (2010). Evaluation of cerebral blood flow changes in
488 focal cerebral ischemia rats by using transcranial Doppler ultrasonography.
489 *Ultrasound Med. Biol.* 36, 595–603.
- 490 Liman, T. G., and Endres, M. (2012). New vessels after stroke: postischemic
491 neovascularization and regeneration. *Cerebrovasc. Dis.* 33, 492–499.
- 492 Lin, C.-Y., Siow, T. Y., Lin, M.-H., Hsu, Y.-H., Tung, Y.-Y., Jang, T., et al. (2013).
493 Visualization of rodent brain tumor angiogenesis and effects of antiangiogenic
494 treatment using 3D $\Delta R2$ - μ MRA. *Angiogenesis* 16, 785–793.
- 495 Lowerison, M. R., Sekaran, N. C., Zhang, W., Dong, Z., Chen, X., Llano, D. A., et al. (2021).
496 Aging-related cerebral microvascular changes visualized using Ultrasound
497 Localization Microscopy in the living mouse. *bioRxiv*.
498 doi:10.1101/2021.06.04.447141.
- 499 Macé, E., Montaldo, G., Cohen, I., Baulac, M., Fink, M., and Tanter, M. (2011). Functional
500 ultrasound imaging of the brain. *Nature methods* 8, 662–664.
- 501 Macé, E., Montaldo, G., Osmanski, B.-F., Cohen, I., Fink, M., and Tanter, M. (2013).
502 Functional ultrasound imaging of the brain: theory and basic principles. *IEEE Trans.*
503 *Ultrason. Ferroelectr. Freq. Control* 60, 492–506.
- 504 Macé, É., Montaldo, G., Trenholm, S., Cowan, C., Brignall, A., Urban, A., et al. (2018).
505 Whole-Brain Functional Ultrasound Imaging Reveals Brain Modules for Visuomotor
506 Integration. *Neuron* 100, 1241-1251.e7.
- 507 Meyer, E. P., Ulmann-Schuler, A., Staufenbiel, M., and Krucker, T. (2008). Altered
508 morphology and 3D architecture of brain vasculature in a mouse model for
509 Alzheimer's disease. *Proc. Natl. Acad. Sci. U. S. A.* 105, 3587–3592.
- 510 Nouhoum, M., Ferrier, J., Osmanski, B.-F., Ialy-Radio, N., Pezet, S., Tanter, M., et al. (2021).
511 A functional ultrasound brain GPS for automatic vascular-based neuronavigation. *Sci.*
512 *Rep.* 11, 15197.
- 513 Pathak, A. P., Kim, E., Zhang, J., and Jones, M. V. (2011). Three-dimensional imaging of the
514 mouse neurovasculature with magnetic resonance microscopy. *PLoS One* 6, e22643.
- 515 Pétrault, O., Pétrault, M., Ouk, T., Bordet, R., Bérézowski, V., and Bastide, M. (2019).
516 Visceral adiposity links cerebrovascular dysfunction to cognitive impairment in middle-
517 aged mice. *Neurobiol. Dis.* 130, 104536.
- 518 Rungta, R. L., Zuend, M., Aydin, A.-K., Martineau, É., Boido, D., Weber, B., et al. (2021).
519 Diversity of neurovascular coupling dynamics along vascular arbors in layer II/III
520 somatosensory cortex. *Commun. Biol.* 4, 855.
- 521 Sans-Dublanc, A., Chrzanowska, A., Reinhard, K., Lemmon, D., Nuttin, B., Lambert, T., et al.
522 (2021). Optogenetic fUSI for brain-wide mapping of neural activity mediating
523 collicular-dependent behaviors. *Neuron*. doi:10.1016/j.neuron.2021.04.008.

- 524 Shih, A. Y., Driscoll, J. D., Drew, P. J., Nishimura, N., Schaffer, C. B., and Kleinfeld, D.
525 (2013). Two-photon microscopy as a tool to study blood flow and neurovascular
526 coupling in the rodent brain. *J. Cereb. Blood Flow Metab.* 33, 319–319.
- 527 Sieu, L.-A., Bergel, A., Tiran, E., Deffieux, T., Pernot, M., Gennisson, J.-L., et al. (2015). EEG
528 and functional ultrasound imaging in mobile rats. *Nat. Methods* 12, 831–834.
- 529 Szu, J. I., and Obenaus, A. (2021). Cerebrovascular phenotypes in mouse models of
530 Alzheimer’s disease. *J. Cereb. Blood Flow Metab.* 41, 1821–1841.
- 531 Takahashi, D. Y., El Hady, A., Zhang, Y. S., Liao, D. A., Montaldo, G., Urban, A., et al.
532 (2021). Social-vocal brain networks in a non-human primate. *bioRxiv*.
533 doi:10.1101/2021.12.01.470701.
- 534 Tetteh, G., Efremov, V., Forkert, N. D., Schneider, M., Kirschke, J., Weber, B., et al. (2020).
535 DeepVesselNet: Vessel segmentation, centerline prediction, and bifurcation detection
536 in 3-D angiographic volumes. *Front. Neurosci.* 14, 592352.
- 537 Todorov, M. I., Paetzold, J. C., Schoppe, O., Tetteh, G., Shit, S., Efremov, V., et al. (2020).
538 Machine learning analysis of whole mouse brain vasculature. *Nat. Methods* 17, 442–
539 449.
- 540 Urban, A., Brunner, C., Dussaux, C., Chassoux, F., Devaux, B., and Montaldo, G. (2015a).
541 Functional Ultrasound Imaging of Cerebral Capillaries in Rodents and Humans.
542 *Jacobs Journal of Molecular and Translational Medicine* 1, 007.
- 543 Urban, A., Dussaux, C., Martel, G., Brunner, C., Mace, E., and Montaldo, G. (2015b). Real-
544 time imaging of brain activity in freely moving rats using functional ultrasound. *Nature*
545 *methods* 12, 873–878.
- 546 Urban, A., Mace, E., Brunner, C., Heidmann, M., Rossier, J., and Montaldo, G. (2014).
547 Chronic assessment of cerebral hemodynamics during rat forepaw electrical
548 stimulation using functional ultrasound imaging. *Neuroimage* 101, 138–149.
- 549 Vidal, B., Droguerre, M., Venet, L., Valdebenito, M., Mouthon, F., Zimmer, L., et al. (2021).
550 Inter-subject registration and application of the SIGMA rat brain atlas for regional
551 labeling in functional ultrasound imaging. *J. Neurosci. Methods* 355, 109139.
- 552 Wu, C., Xie, Y., Shao, L., Yang, J., Ai, D., Song, H., et al. (2019). Automatic boundary
553 segmentation of vascular Doppler optical coherence tomography images based on
554 cascaded U-net architecture. *OSA Continuum* 2, 677.
- 555 Yang, P., Pavlovic, D., Waldvogel, H., Draganow, M., Synek, B., Turner, C., et al. (2015).
556 String vessel formation is increased in the brain of Parkinson disease. *J. Parkinsons*.
557 *Dis.* 5, 821–836.
- 558 Yousefi, S., Liu, T., and Wang, R. K. (2015). Segmentation and quantification of blood
559 vessels for OCT-based micro-angiograms using hybrid shape/intensity compounding.
560 *Microvasc. Res.* 97, 37–46.
- 561 Zhang, X., Yin, X., Zhang, J., Li, A., Gong, H., Luo, Q., et al. (2019). High-resolution mapping
562 of brain vasculature and its impairment in the hippocampus of Alzheimer’s disease
563 mice. *Natl. Sci. Rev.* 6, 1223–1238.
- 564